International Journal of Nanomedicine

Dovepress
Taylor & Francis Group

Open Access Full Text Article

ORIGINAL RESEARCH

$Cu_2(OH)PO_4$@PAA Nanoparticles for Highly Effective Combination of Chemodynamic, Photodynamic and Photothermal Therapies Against Bladder Cancer

Yadong Liu[1,2,*], Huiyan Lv[3,*], Yaodong Chen[4,*], Shazhou Ye[1], Zhong Zheng[1], Lei Chen[1], Zejun Yan[1], Xingyi Li[5]

[1]Department of Urology, The First Affiliated Hospital of Ningbo University, Ningbo, Zhejiang, People's Republic of China; [2]State Key Laboratory of Ultrasound in Medicine and Engineering, The Second Affiliated Hospital of Chongqing Medical University, Chongqing, People's Republic of China; [3]Department of Nephrology, the First Affiliated Hospital of Harbin Medical University, Harbin, Heilongjiang, People's Republic of China; [4]Department of Ultrasonic Imaging, First Hospital of Shanxi Medical University, Taiyuan, Shanxi, People's Republic of China; [5]Department of Ultrasonic Imaging, The First Affiliated Hospital of Ningbo University, Ningbo, Zhejiang, People's Republic of China

*These authors contributed equally to this work

Correspondence: Xingyi Li; Zejun Yan, Email fyylixingyi@nbu.edu.cn; fyyyanzejun@nbu.edu.cn

---

Background: Due to the complex structure and variable microenvironment in the progression of bladder cancer, the efficacy of traditional treatment methods such as surgery and chemotherapy is limited. Tumor residual, recurrence and metastasis are still difficult to treat. The integration of diagnosis and treatment based on nanoparticles can offer the potential for precise tumor localization and real-time therapeutic monitoring. Photodynamic therapy (PDT), which generates reactive oxygen species (ROS) under laser irradiation, can be effectively combined with photothermal therapy (PTT) and chemodynamic therapy (CDT) to target non-muscle-invasive bladder tumors. In this study, $Cu_2(OH)PO_4$@PAA nanoparticles with photoacoustic (PA) imaging capabilities were utilized to explore their potential for precise intraoperative tumor identification and multimodal therapy.

Methods: The generation of ROS was detected to evaluate the potential of PDT and copper ion-induced CDT. Additionally, the PA imaging capability and biosafety of the nanoparticles were systematically evaluated. Finally, the anti-tumor efficacy of $Cu_2(OH)PO_4$@PAA-mediated CDT/PDT/PTT and the underlying mechanisms were assessed in vitro and in vivo.

Results: $Cu_2(OH)PO_4$@PAA could implement the CDT effect through a Cu^+-induced Fenton-like reaction and substantial consumption of glutathione (GSH). Besides, $Cu_2(OH)PO_4$@PAA could execute NIR-I-triggered PDT by generating $^1O_2$ and thermal images showed that $Cu_2(OH)PO_4$@PAA has the potential to perform PTT through light-heat energy conversion. $Cu_2(OH)PO_4$@PAA possessed dose-dependent PA signal transduction ability. Without laser exposure, $Cu_2(OH)PO_4$@PAA weakened cell viability, induced apoptosis, and suppressed epithelial-mesenchymal transition (EMT) by exhibiting the CDT effect alone. However, after the introduction of PDT and/or PTT, the above anti-tumor effects were significantly enhanced.

Conclusion: This study systematically explores the combined anti-cancer mechanisms from the perspective of epithelial-mesenchymal transition, providing a theoretical and technical foundation for bladder cancer treatment.

Keywords: $Cu_2(OH)PO_4$@PAA, chemodynamic therapy, photodynamic therapy, photothermal therapy, bladder cancer

---

Introduction

Approximately 75% of newly diagnosed bladder cancer (BC) lesions are confined to the mucosa or submucosa, indicating absence of muscle involvement. These tumors are classified as non-muscle-invasive bladder cancers (NMIBC). The endophytic growth pattern of BC into the vesical lumen, coupled with the bladder's anatomical communication with the exterior through the urethra, creates clinical characteristics resembling superficial tumors and

Received: 5 June 2025
Accepted: 22 August 2025
Published: 1 September 2025

enables transurethral therapeutic approaches.[1] Transurethral resection of bladder tumor (TURBT) is the standard treatment strategy recommended by the international guidelines for NMIBC. Presently, both thulium laser and holmium laser have emerged as effective alternatives for transurethral bladder tumor resection. This surgical procedure remains highly dependent on the surgeon's experience and intraoperative visual assessment.[2] However, it is difficult for surgeons to identify small tumors and distinguish the boundary between benign and malignant tissues under cystoscopy, resulting in misdiagnosis of the tumor and incomplete resection of lesion sites.[3,4] Despite the limitations of traditional surgical methods, the 5-year survival rate of patients with NMIBC can reach 90%. However, the 5-year recurrence rate is as high as 31–78%, and 1–45% of NIMBC cases develop muscle-invasive bladder cancer (MIBC) within 5 years.[5,6] Considering that surgical resection may lead to tumor cell dissemination and implantation, post-surgery intravesical infusion of chemotherapeutic drugs, such as epirubicin, gemcitabine, and mitomycin C, has been explored to prevent tumor recurrence and potential progression. Nevertheless, drug resistance, urine dilution, and limited penetration into tumor tissues are among the key factors that restrict the efficacy of intravesical chemotherapy.[2,5,7] Therefore, identifying a method for intraoperative determination of tumor localization and depth, as well as a minimally invasive treatment, has become an urgent task.

Recently, phototherapy, including photothermal therapy (PTT) and photodynamic therapy (PDT), has emerged as a prominent research field. PTT relies on photothermal transduction agents (PTA), which are near-infrared (NIR)-absorbing nanomaterials that convert light energy into heat. This process elevates the temperature at the tumor site, leading to destructive death of tumor cells.[8] In contrast, the therapeutic mechanism of PDT focuses on the generation of reactive oxygen species (ROS) by photosensitizers (PSs) via energy transfer upon external light irradiation.[9] Given the characteristic growth pattern of BC and the unique anatomical features of the bladder, NMIBC exhibits properties analogous to superficial lesions, making it particularly suitable for PDT and PTT. Despite the unparalleled advantages of PDT and PTT, such as their noninvasive nature, minimal toxicity to surrounding healthy tissues, and adjustable laser irradiation treatment intensity, each modality has inherent limitations. For instance, the hypoxic environment of tumor tissues and limited penetration of external light hinders the continuous generation of ROS, thereby reducing the efficacy of PDT.[9–11] The heat shock response induced by hyperthermia can undermine the therapeutic effect of PTT by inhibiting tumor cells.[12] Consequently, combining PTT, PDT, and other treatment strategies to maximize the therapeutic effect and overcome the limitations of monotherapy has become a key focus of recent research.

Since the depletion of ROS is the culprit for the deterioration of PDT efficacy, some attempts have been made to utilize another ROS-involved chemodynamic therapy (CDT) to synergistically strengthen the biomolecular destruction, apoptosis, and oxidative damage of tumor cells.[13,14] The realization of CDT utilizes the Fenton effect of multifunctional metal ions, such as Fe^{3+}, Cu^{2+} and $Mn^{2+,}$ which can catalyze the conversion of less cytotoxic hydrogen peroxide (H_2O_2) into highly cytotoxic hydroxyl radicals (•OH).[15,16] Unlike PDT, CDT does not require external light irradiation, thereby significantly reducing energy loss caused by tissue penetration. Moreover, the continuous generation of •OH alters the intracellular redox state, which can strengthen the oxidative damage capability of singlet oxygen ($^1O_2$), the core molecule of PDT.[15,17,18] Thus, based on the above findings, we aimed to synthesize metal-ion-based nanoparticles with NIR absorption capacity. This material will serve as a ROS generator to achieve trifunctional synergistic therapy by combining CDT, PTT, and PDT. Therapeutic effects are realized through the metal-induced Fenton effect, localized hyperthermia generated by light irradiation, and laser-induced $^1O_2$ generation.

$Cu_2(OH)PO_4$ is a promising candidate for trifunctional anti-tumor therapy.[19] First, its optical absorption spectrum spans the range of 800–1400 nm, which is aligned with the irradiation window for NIR irradiation-induced PTT. Second, $Cu_2(OH)PO_4$ has been previously demonstrated to generate ROS under NIR irradiation and exhibits PDT functionality.[20] Additionally, paramagnetic copper (Cu) is expected to produce CDT through the Cu□-mediated Fenton-like effect.[21] However, the development of $Cu_2(OH)PO_4$-based nanoparticles for anti-tumor biological applications poses several challenges, such as controlling the particle morphology and modifying the surface structures. Fortunately, $Cu_2(OH)PO_4$ nanoparticles coated with polyacrylic acid (PAA), exhibited excellent PDT and PTT effects. More importantly, the excellent NIR absorption performance of the copper (a paramagnetic ion with an unpaired 3d electron)-based nanomaterial suggests its potential as a bioimaging diagnostic agent. Under laser irradiation, $Cu_2(OH)PO_4$@PAA can visualize tumor sites through photoacoustic imaging (PA), enabling highly precise tumor treatment.[20]

In this study, we successfully fabricated $Cu_2(OH)PO_4$@PAA using a hydrothermal method following established protocols and explored its application in the treatment of BC (Figure 1A). A series of cellular and animal experiments confirmed that $Cu_2(OH)PO_4$@PAA exhibited real-time PA bioimaging ability and CDT/PTT/PDT synergistic therapeutic functions. In addition, as a single-component theranostic nanoparticle, $Cu_2(OH)PO_4$@PAA not only simplifies the synthetic process but also avoids the drawbacks of multicomponent nanosystems, such as poor stability and mutual interference. Additionally, the biocompatibility of $Cu_2(OH)PO_4$@PAA was thoroughly investigated, and its excellent biocompatibility highlights its potential for clinical translation (Figure 1B). In summary, this study presents a novel and feasible theranostic strategy for BC treatment.

Materials and Methods

Experimental Reagents

The CCK-8 assay kit was purchased from Dojindo Laboratories (Kumamoto, Japan). $Cu(NO_3)_2 \cdot 3H_2O$ and $Na_2HPO_4 \cdot 12H_2O$ were obtained from Sinopharm Chemical Reagent Co. LTD (Shanghai, China). Poly (acrylic acid) sodium salt (PAA) and Methylene Blue Solution (MB) were acquired from Sigma-Aldrich (Merck KGaA, Germany). Calcein/PI Cell Activity and Cytotoxicity Test Kit and Reactive Oxygen Species Assay Kit (DCFH-DA) were purchased from Beyotime Biotechnology (Shanghai, China). The Annexin V-FITC/PI Apoptosis Detection Kit was obtained from Multi Science (Hangzhou, China). 1,3-biphenyl isocoumarin-2,5-diphenyl-3,4-benzofuran (DPBF) was purchased from Damas Beta (Shanghai, China). All immunoassay-related fluorescent and histochemical antibodies were purchased from the Servicebio Company (Wuhan, China). 3,3,5,5-tetramethylbenzidine (TMB) and 5,5-dithiobis (2-nitrobenzoic acid)

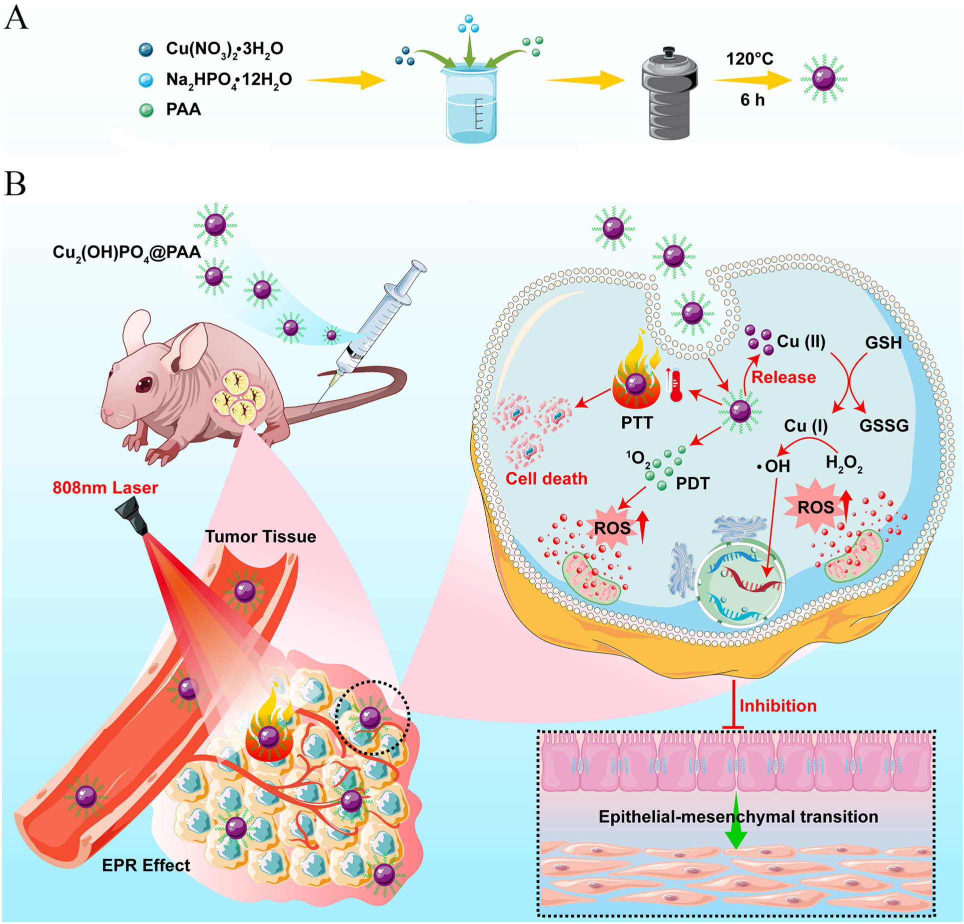

Figure 1 Schematic illustration of (**A**) the synthetic procedure of $Cu_2(OH)PO_4$@PAA and (**B**) the corresponding CDT, PDT and PTT treatment for bladder cancer.

(DTNB) were acquired from MACKLIN Biochemical Technology (Shanghai, China). BALB/c nude mice were purchased from the CAVENS Laboratory Animal Co., Ltd. (Changzhou, China).

Synthesis of $Cu_2(OH)PO_4$@PAA

$Cu_2(OH)PO_4$@PAA nanoparticles was fabricated via a hydrothermal method following previously reported protocols.[20] Briefly, 0.15 g of PAA and 0.29 g of $Cu(NO_3)_2·3H_2O$ were dissolved in 30 mL of distilled water under magnetic stirring. Subsequently, 30 mL of $Na_2HPO_4·12H_2O$ solution (7.13 mg/mL) was slowly dripped into the mixed light-blue solution under continuous magnetic stirring for 15 min. The pH of the final suspension was adjusted to 7.0 using NaOH solution. The mixture was then transferred to a 100 mL Teflon-lined autoclave and heated in an electric oven at 120 °C for 6 h. The cyan product was centrifuged (8000 rpm, 5 min) and washed with deionized water and ethanol. Finally, the $Cu_2(OH)PO_4$@PAA nanoparticles were homogeneously resuspended in deionized water using an ultrasonic dispersion method.

Characterization

The morphology and structure of $Cu_2(OH)PO_4$@PAA were characterized using transmission electron microscopy (TEM, FEI, Tecnai G2 F30, USA) and scanning electron microscopy (SEM, SU8020, Japan). The zeta potential and particle size of the samples were determined using a particle size and zeta potential analyzer (NanoBrook Omni, Brookhaven Instruments. Ltd, UK). Optical properties were determined using a UV-3600 spectrophotometer (Hitachi, Tokyo, Japan).

Depletion of Glutathione

The consumption of glutathione (GSH) was used to reflect the degree of reduction of copper ions (II) in the $Cu_2(OH)PO_4$@PAA nanoparticles. The $Cu_2(OH)PO_4$@PAA aqueous solution (64 µg/mL) was reacted with GSH (5 mM) in PBS (1 mL, pH 5.5). Next, DTNB (10 µL, 3.96 mg/mL) was added to the mixed solution and the absorbance at 412 nm was measured using ultraviolet-visible spectroscopy after 0, 4, 8, 12, 24, and 48 h of reaction.

Detection of Hydroxyl Radicals

The hydroxyl radical (·OH) generation was detected using TMB as a probe. Briefly, solutions of PBS (pH 5.5) containing TMB (20 µL, 9.8 mg/mL) and H_2O_2 (200 µL, 0.1 mM) with $Cu_2(OH)PO_4$@PAA (64 and 128 µg/mL), or without $Cu_2(OH)PO_4$@PAA were prepared. Changes in absorbance at 652 nm were monitored after 1 h. Additionally, the generation of ·OH was detected using UV spectroscopy at reaction times of 0, 0.5, 1, 2, and 4 h.

Furthermore, the OH generated by laser irradiation was detected by MB. After the $Cu_2(OH)PO_4$@PAA solution containing MB was irradiated with a laser (2 W) for 0, 5, 10, 15, 20, 25, and 30 min or irradiated by lasers of different powers (0.5, 1, 1.5, and 2 W) for 10 min, the absorbance changes at 652 nm were monitored by UV spectroscopy.

Detection of Singlet Oxygen

The generation of $^1O_2$ was detected using DPBF. Twenty microliters of DPBF (1 mg/mL) were added to 500 µL of $Cu_2(OH)PO_4$@PAA (0.5 mg/mL) or deionized water. The two mixed systems were then laser-irradiated at 808 nm for 0, 5, 10, 15, 20, 25, and 30 min. In addition, the mixed system was irradiated for 10 min at different powers (0.5, 1, 1.5, and 2 W). In addition, different concentrations of $Cu_2(OH)PO_4$@PAA (0.0625, 0.125, 0.25, 0.5, and 1 mg/mL) were irradiated using a laser (2 W) for 10 min. Changes in absorbance at 410 nm were monitored to determine the generation of $^1O_2$.

Evaluation of Photothermal Characteristics in vitro

The photothermal properties of $Cu_2(OH)PO_4$@PAA were evaluated at concentrations of 0.0625, 0.125, 0.25, 0.5, and 1 mg/mL under Near-Infrared-I (NIR-I) irradiation (808 nm, 2 W/cm^2). Furthermore, $Cu_2(OH)PO_4$@PAA aqueous solution (0.5 mg/mL) was also treated by different irradiation powers from 0.5 W to 2 W. An infrared thermal imaging camera (Fotric 226; Wenzhou Valvespro Flow Control Technology Co., Ltd. Zhejiang, China) was used to capture the temperature changes.

Cytotoxicity Evaluation in vitro

The cellular uptake of $Cu_2(OH)PO_4$@PAA nanoparticles was detected using biological transmission electron microscopy (TEM). To further validate cellular internalization of $Cu_2(OH)PO_4$@PAA nanoparticles, MB49 cells (Otwo Biotech Inc. cat #: HTX2716, Guangzhou, China) were incubated with the nanoparticles for 0.5, 1, 2, and 4 h. Following thorough removal of non-internalized particles through washing, cells were trypsinized and pelleted by centrifugation. The resulting cell precipitates were then subjected to inductively coupled plasma-optical emission spectrometry (ICP-OES) analysis to quantify intracellular copper content across experimental group.

The cell viability in the experimental groups after different treatments was evaluated using the CCK-8 assay. Briefly, MB49 cells were seeded in a 96-well plate and incubated with various concentrations of $Cu_2(OH)PO_4$@PAA solution (8, 16, 32, 64, 128, 256, and 512 μg/mL) without laser irradiation. Cell viability was measured after 4 h and 24 h of incubation. HUVEC were treated using the aforementioned method to determine a relatively safe concentration. In control group, the MB49 cells were neither treated with nanoparticles nor subjected to laser irradiation. The laser group was treated with an 808 nm laser (2 W/cm^2, 10 min) without nanoparticle incubation. In the CDT group, MB49 cells were incubated with 128 μg/mL $Cu_2(OH)PO_4$@PAA without laser irradiation to investigate the copper ion-mediated single CDT effect. For the CDT/PDT and CDT/PTT groups, MB49 cells were incubated with 128 μg/mL $Cu_2(OH)PO_4$@PAA and subjected to 808 nm laser irradiation on ice (2 W/cm^2), maintaining the temperature below 42 °C for 10 min under the monitoring of an infrared imaging system (CDT/PDT group), or irradiated at 2 W/cm^2 for 10 min (CDT/PTT group). After each treatment, cell viability was measured using the CCK-8 assay.

Live-Dead Cell Staining Assay

A live-dead cell staining assay was also conducted to evaluate cell viability. Briefly, MB49 cells were seeded in 3.5 cm cell culture dishes and incubated for 24 h. The cells were then randomly divided into five groups (control, laser, CDT, CDT/PDT, and CDT/PTT groups). After treatment, the cells were washed thrice with PBS and incubated with calcein-AM (3 μL) and propidium iodide (PI, 3 μL) for 30 min. The cells were then washed thrice with PBS and observed under a fluorescence microscope. Live and dead cells were stained with green and red, respectively.

Cell Apoptosis Analysis

The treatment protocol for apoptosis detection was consistent with that described for the live-dead cell staining assay. After the corresponding treatment of all groups, the cells were trypsinized, centrifuged, resuspended in PBS, and incubated with Annexin V-FITC/PI for 5 min in the dark at 37 °C. Subsequently, flow cytometry was used to analyze cell samples to distinguish between apoptotic and necrotic cells.

Detection of ROS Levels

DCFH-DA was used as an indicator of cellular ROS levels. MB49 cells were seeded in 6-wells plates (1×10^5 cells/well) and randomly divided into five groups: control, laser, CDT, CDT/PDT, and CDT/PTT groups. The cells in the above groups were treated as described for the live-dead cell staining assay. The cells in each group were stained with DCFH-DA in a 37 °C incubator for 30 min. Subsequently, the cells were washed thrice with PBS and observed under a fluorescence microscope. ROS levels are indicated by green fluorescence. Flow cytometry was used to quantitatively assess cellular ROS levels.

Cellular Immunofluorescence

Cellular immunofluorescence was conducted to evaluate the effect of $Cu_2(OH)PO_4$@PAA on epithelial-mesenchymal transition (EMT) in MB49 cells. MB49 cells seeded in 24-well plates were randomly divided into five groups: control, laser, CDT, CDT/PDT, and CDT/PTT. As previously mentioned, each group was treated with or without $Cu_2(OH)PO_4$@PAA nanoparticles and/or different laser irradiation. Treated cells were fixed with 4% formalin, permeabilized with Triton X-100, and blocked with 1% bovine serum albumin (BSA) for 1 h. After washing thrice with PBS, MB49 cells in each group were incubated with Anti-Vimentin Rat monoclonal antibody (mAb) or Anti-E-cadherin Mouse mAb, followed by incubation with a FITC-conjugated secondary antibody. The nuclei of MB49 cells were counterstained with DAPI and immunofluorescence images were acquired using a fluorescence microscope.

Photoacoustic Imaging in vitro and in vivo

The photoacoustic (PA) capability of $Cu_2(OH)PO_4$@PAA was assessed using a Vevo LAZR imaging system (Visual Sonics Inc., Toronto, ON, Canada). To determine the optimal excitation wavelength, the maximum absorbance of $Cu_2(OH)PO_4$@PAA was measured in the 680–970 nm range. In vitro experiments, $Cu_2(OH)PO_4$@PAA aqueous solutions were diluted to concentrations ranging from 0.03125 mg/mL to 0.5 mg/mL. PA imaging was then performed on these dilutions and the corresponding PA intensities were recorded. For in vivo PA imaging, MB49 tumor-bearing mice were intravenously injected with $Cu_2(OH)PO_4$@PAA suspension (1 mg/mL, 100 μL) through the tail vein. The tumor regions were then imaged at different time points (0, 2, 4, 8, 12, and 24 h post-injection) using ultrasonic testing and the PA imaging system.

In vivo Photothermal Performance of $Cu_2(OH)PO_4$@PAA

All protocols used in the study were established seriously subject to guideline of Animal Ethics Committee and approved by the ethics committee of The Second Affiliated Hospital of Chongqing Medical University. The photothermal conversion performance of $Cu_2(OH)PO_4$@PAA was evaluated in tumor-bearing mice. Saline (100 μL) and $Cu_2(OH)PO_4$@PAA aqueous dispersion (1 mg/mL, 100 μL) were injected intravenously into mice. At 4 h post-injection, the tumor tissues in the CDT/PTT group were irradiated with an 808 nm laser at 1.5 W/cm^2 for 6 min. In contrast, the tumor tissues in the CDT/PDT group were subjected to intermittent irradiation (1.5 W/cm^2). The irradiation was paused when the temperature reached 42 °C, and then resumed after cooling to room temperature, with the effective irradiation time lasting for 6 minutes. Temperature changes in the tumor region and infrared (IR) thermal images were monitored using an IR thermal imaging camera at different time points.

CDT/PDT/PTT Anti-Tumor Therapy in vivo

The effects of $Cu_2(OH)PO_4$@PAA-mediated CDT, PDT and PTT on the primary tumors were then evaluated in vivo. MB49 cells (5×10^5) suspended in 100 μL of PBS were subcutaneously injected into the flanks of BALB/c nude mice to establish a tumor xenograft transplantation model. After 7 days of logarithmic growth, MB49 tumor-bearing nude mice (n = 25) were randomly divided into five groups: control (saline), laser, CDT, CDT/PDT, and CDT/PTT. On days 1 and 4, mice in the CDT, CDT/PDT, and CDT/PTT groups were intravenously injected with $Cu_2(OH)PO_4$@PAA nanoparticle aqueous solution (1 mg/mL, 100 μL), whereas mice in the control and laser groups were injected with saline solution only. Four hours post-injection, mice in laser group were irradiated with 808 nm laser irradiation at 1.5 W/cm^2 for 10 min, mice in CDT/PDT group were irradiated by 808 nm laser under real-time temperature monitoring to ensure that the maximum temperature did not exceed 42 °C, with a total effective irradiation duration of 10 min. Mice in the CDT/PTT group were irradiated with an 808 nm laser at 1.5 W/cm^2 for 10 min. Body weight and tumor size were measured every other day during the 10-day observation period. Tumor size was measured with the digital caliper, and the tumor volume was estimated with this formula: $0.5 \times \text{length} \times \text{width}^2$ (V_0: initial tumor volume before treatment). On day 10, all mice were euthanized and tumor tissues were collected for further H&E staining and immunohistochemical analysis of E-cadherin and Vimentin expression. Proliferation and apoptosis of tumor tissues were assessed using proliferating cell nuclear antigen (PCNA) and terminal deoxynucleotidyl transferase dUTP nick end (TUNEL) staining.

Evaluation of Biosafety in vivo

To estimate the biocompatibility of $Cu_2(OH)PO_4$@PAA in vivo, mice were injected with $Cu_2(OH)PO_4$@PAA solution (1 mg/mL, 100 μL) via the tail vein. All mice injected with nanoparticles were randomly euthanized at 1, 3, 5, 7, and 14 days post-injection. Non-injected mice were used as controls. On the day of sacrifice, blood was collected for biochemical analysis, including alanine aminotransferase (ALT), creatinine, and total bilirubin (TBIL), as well as for hematological analysis, including red blood cell count, mean corpuscular hemoglobin concentration (MCHC), platelet count (PLT), plateletcrit (PCT), mean platelet volume (MPV), and the percentage of neutrophils and lymphocytes. The major organ tissues were harvested and sectioned for histological analysis by H&E staining.

Statistical Analysis

All statistical analyses were performed using SPSS software (version 22.0). All data are presented as mean ± standard deviation (SD). The significance of the differences was analyzed using one-way analysis of variance (ANOVA) and Student's *t*-test. Statistical significance was set at $p < 0.05$.

Results

Characterization of $Cu_2(OH)PO_4$@PAA

PAA-modified $Cu_2(OH)PO_4$ was synthesized using a hydrothermal method. TEM and SEM revealed the spherical morphology and particle size distribution of $Cu_2(OH)PO_4$@PAA (Figure 2A and B). Elemental mapping demonstrated that Cu and P were uniformly distributed throughout the spatial structure of the $Cu_2(OH)PO_4$@PAA nanoparticles (Figure 2C). The average size of $Cu_2(OH)PO_4$@PAA was 178 nm, whereas that of unmodified $Cu_2(OH)PO_4$ was 18164 nm (Figure 2D). The zeta potential values of $Cu_2(OH)PO_4$@PAA and $Cu_2(OH)PO_4$ particles were −15.94 mV and −10.45 mV, respectively (Figure 2E). The absorbance spectrum of $Cu_2(OH)PO_4$@PAA ranged from 650 to 900 nm (Figure 2F), indicating its potential as an effective absorber for NIR I irradiation-induced PTT. Figure 2G illustrates the hemolysis of different concentrations of $Cu_2(OH)PO_4$@PAA nanoparticles in PBS and deionized water, demonstrating their excellent biocompatibility. As shown in Figure 2H, unmodified $Cu_2(OH)PO_4$ nanoparticles were insoluble in deionized water and were rapidly deposited at the bottom of the centrifuge tube, suggesting a limited potential for reaching tumor sites via blood circulation. In contrast, the $Cu_2(OH)PO_4$@PAA nanoparticles were homogeneously dispersed in deionized water and formed a milky-blue aqueous suspension, suggesting that surface decoration with PAA endowed these nanoparticles with favorable structural stability and was more conducive to the biological effects of these particles.

CDT, PDT and PTT Properties of Nanoparticles

Glutathione (GSH), which is a key component of the endogenous antioxidant system, plays a critical role in neutralizing.[22] Since Cu^{2+} is reduced to Cu^+ by consuming GSH, the detection of GSH depletion in PBS solution (pH 5.5) treated with $Cu_2(OH)PO_4$@PAA can reflect the ROS-generating capacity of the nanoparticles. This is essential for ROS-dependent anti-tumor mechanisms, including CDT ($Cu^{2+} + GSH \rightarrow Cu^+ + GSSG$, $Cu^+ + H_2O_2\ Cu^{2+} + \bullet OH$), and PDT. We incubated a PBS solution containing GSH and $Cu_2(OH)PO_4$@PAA aqueous suspensions for varying durations and then detected GSH consumption using DTNB probes. The results revealed a clear time-dependent decrease in the absorption of DTNB at approximately 412 nm (Figure 2I). These results demonstrate that $Cu_2(OH)PO_4$@PAA nanoparticles have the ability to consume GSH in a time-dependent manner, which contributes to the maintenance of high intracellular ROS levels. To further investigate the Cu^+-mediated •OH generation and evaluate the CDT properties of $Cu_2(OH)PO_4$@PAA, 3,3,5,5-tetramethylbenzidine (TMB) was utilized as an indicator of the •OH produced via a Fenton-like reaction. The oxidation of TMB by •OH results in a gradual color change from colorless to blue, accompanied by a distinct absorption peak at 652 nm. Compared with the TMB/H_2O_2 group, the absorption at 652 nm was significantly enhanced in the TMB/H_2O_2/$Cu_2(OH)PO_4$@PAA group, exhibiting a clear concentration-dependent trend (Figure 2J). This indicates that the increased release of copper from $Cu_2(OH)PO_4$@PAA promotes the conversion of H_2O_2 into •OH. Meanwhile, as shown in Figure 2K, the absorption peak of TMB increased dramatically in a time-dependent manner, further confirming the favorable CDT effect of $Cu_2(OH)PO_4$@PAA through the Fenton-like reaction. The characteristic absorbance of $Cu_2(OH)PO_4$@PAA in the NIR region indicates its potential for PTT treatment. Therefore, the photothermal performance of $Cu_2(OH)PO_4$@PAA in vitro was systematically studied. The photothermal conversion of $Cu_2(OH)PO_4$@PAA nanoparticles was assessed at various laser power densities (0.5, 1.0, 1.5 and 2.0 W/cm^2) and nanoparticle concentrations (0.0625, 0.125, 0.25, 0.5 and 1 mg/mL). Obvious concentration-dependent (Figure 3A) and laser-power-dependent (Figure 3B) PTT performances were observed. In addition, under NIR-I laser irradiation, the photothermal efficiency of $Cu_2(OH)PO_4$@PAA did not significantly decline after five cycles of heating/cooling (Figure 3C), demonstrating its excellent photothermal stability in NIR-I-triggered tumor hyperthermia. Since PDT depends on the photogeneration of ROS, especially $^1O_2$ and ·OH, we utilized DPBF and MB as the indicator to detect the level of $^1O_2$ and ·OH generated by $Cu_2(OH)PO_4$@PAA aqueous solution under laser irradiation to

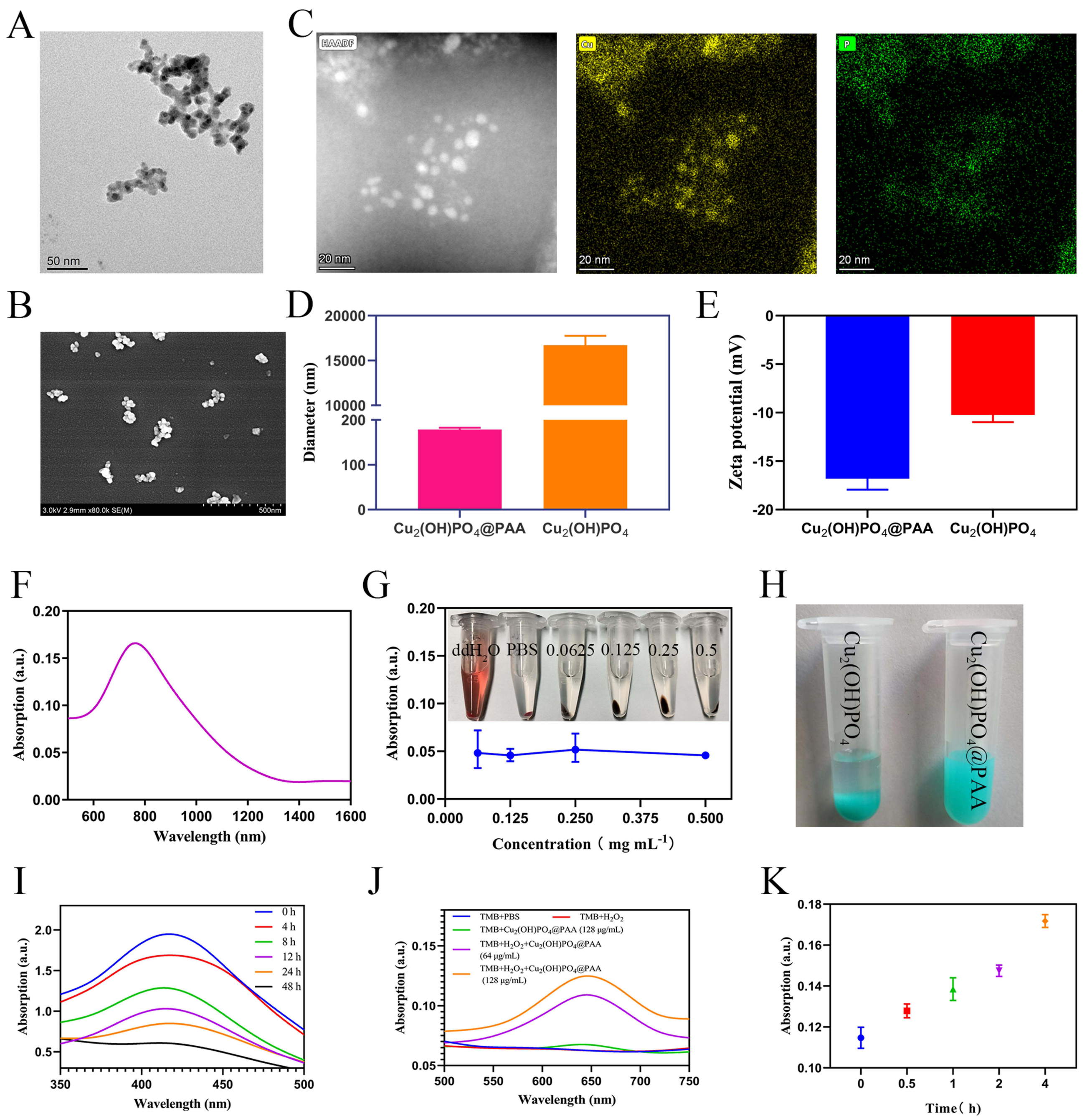

Figure 2 (**A**) TEM images of $Cu_2(OH)PO_4$@PAA nanoparticles. (**B**) SEM images of $Cu_2(OH)PO_4$@PAA nanoparticles. (**C**) Elemental distribution mappings of $Cu_2(OH)PO_4$@PAA. (**D**) Zeta potential of $Cu_2(OH)PO_4$@PAA and $Cu_2(OH)PO_4$. (**E**) Size distribution of $Cu_2(OH)PO_4$@PAA and $Cu_2(OH)PO_4$. (**F**) Absorption spectrum of $Cu_2(OH)PO_4$@PAA. (**G**) Hemolysis of red blood cells incubated with different concentrations of $Cu_2(OH)PO_4$@PAA nanoparticles. (**H**) Appearance of $Cu_2(OH)PO_4$ and $Cu_2(OH)PO_4$@PAA in deionized water. (**I**) Time dependent of GSH consumption via DTNB probes. (**J** and **K**) TMB absorption was used to detect the production of ·OH in each group to evaluate the Fenton-like reaction effect.

evaluate its PDT efficacy. Compared to the negligible decline observed in the pure water group and pure $Cu_2(OH)PO_4$@PAA group, the laser-irradiated $Cu_2(OH)PO_4$@PAA aqueous suspension exhibited a significant time- and concentration-dependent decrease, indicating that $Cu_2(OH)PO_4$@PAA could serve as an excellent photosensitizer for executing NIR-I-triggered PDT by generating $^1O_2$ and ·OH (Figures 3D–F and S1–S4).

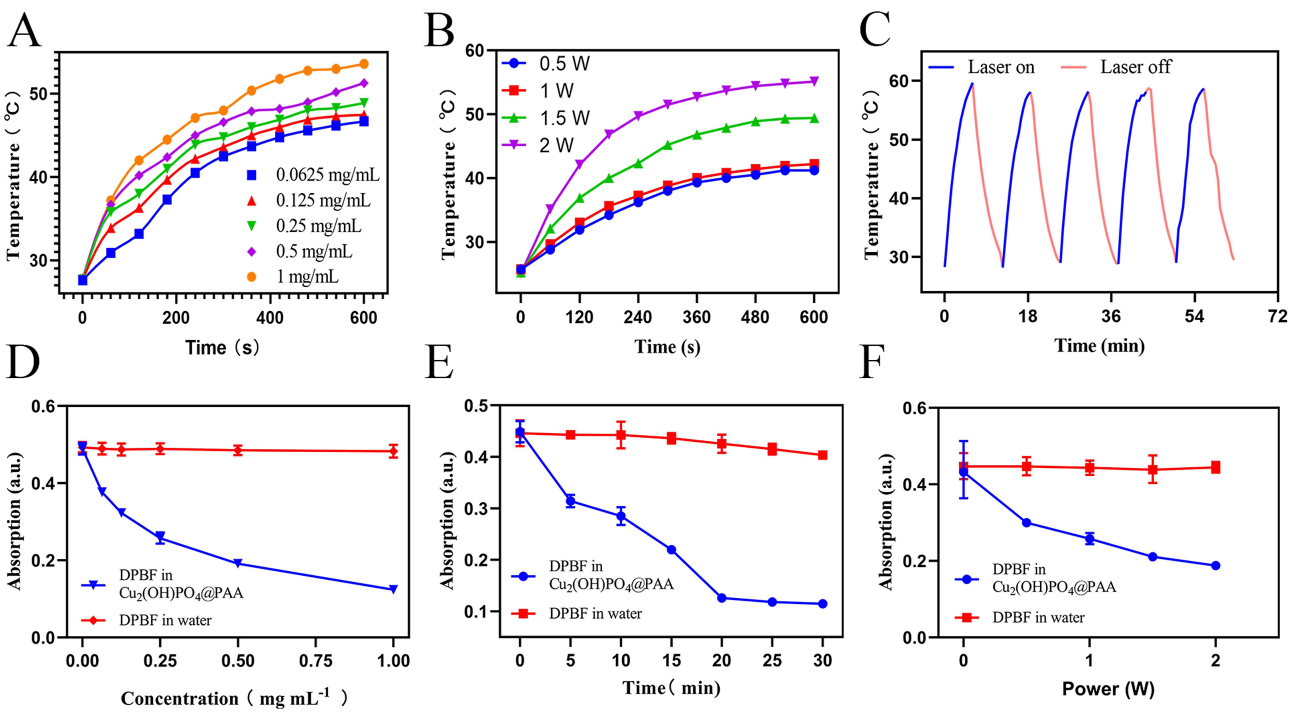

Figure 3 (**A**) Temperature changes of $Cu_2(OH)PO_4$@PAA aqueous suspension at various concentrations under NIR-I irradiation (808 nm, 2 W/cm^2). (**B**) Temperature changes of $Cu_2(OH)PO_4$@PAA aqueous suspension (0.5 mg/mL) at various laser power densities. (**C**) Heating curve of $Cu_2(OH)PO_4$@PAA aqueous suspension under five cycles of heating and cooling processes. (**D**) The absorption spectra of DPBF in aqueous solution and in $Cu_2(OH)PO_4$@PAA suspensions at various concentrations following laser irradiation. (**E** and **F**) The absorption spectra of DPBF after NIR irradiation at various time points and power densities in both aqueous solution and $Cu_2(OH)PO_4$@PAA suspensions.

Anti-Tumor Effect in vitro

Internalization by tumor cells is a prerequisite for the anti-tumor effect of $Cu_2(OH)PO_4$@PAA nanoparticles. After incubating MB49 cancer cells with $Cu_2(OH)PO_4$@PAA for 4 h, the uptake of nanoparticles was observed using TEM (Figure 4A). To further validate the cellular internalization of $Cu_2(OH)PO_4$@PAA nanoparticles, MB49 cells were incubated with the nanoparticles for 0.5, 1, 2, and 4 h. After thoroughly removing non-internalized particles by washing, the cells were trypsinized and pelleted by centrifugation. The resulting cell pellets were subsequently analyzed by ICP-OES to quantify the intracellular copper content across different experimental groups (Figure S5). To evaluate the cytotoxicity mediated by CDT alone, we incubated MB49 cancer cells with various concentrations of $Cu_2(OH)PO_4$@PAA aqueous solution without laser irradiation for 4 and 24 h. The results showed a gradual decline in cell viability with increasing nanoparticle concentration, indicating that $Cu_2(OH)PO_4$@PAA exerts a concentration- and time-dependent cytotoxic effect through CDT (Figures 4B and S6). In addition, in vitro cytotoxicity of $Cu_2(OH)PO_4$@PAA against HUVEC was assessed after 24 h of incubation without laser irradiation (Figure S7). The cytotoxic effect of $Cu_2(OH)PO_4$@PAA on HUVEC was negligible at 128 μg/mL. Therefore, 128 μg/mL was selected as the optimal experimental concentration to ensure biological safety and effective CDT performance. Subsequently, we evaluated the impact of two potential phototherapeutic effects (PDT and PTT) on tumor cells when combined with CDT. By controlling the temperature of the irradiated area, we established two distinct treatment modes, CDT/PDT and CDT/PTT. Compared with the moderate reduction in the CDT group alone, both the CDT/PDT and CDT/PTT groups exhibited a more pronounced decrease in cell viability, particularly when the photothermal properties of these nanoparticles were triggered (Figure 4C). This demonstrates that CDT/PTT combination therapy achieves the strongest anti-tumor effect in vitro. The efficacy of $Cu_2(OH)PO_4$@PAA-mediated CDT/PDT depended on ROS production. Intracellular ROS levels were detected using DCFH-DA as the specific probe. As shown in Figure 4D, the CDT group showed mild green fluorescence signals, whereas the fluorescence signal intensity increased significantly in the CDT/PDT group, confirming that $Cu_2(OH)PO_4$@PAA nanoparticles can generate ROS through Fenton-like reactions, and the photodynamic process leads to

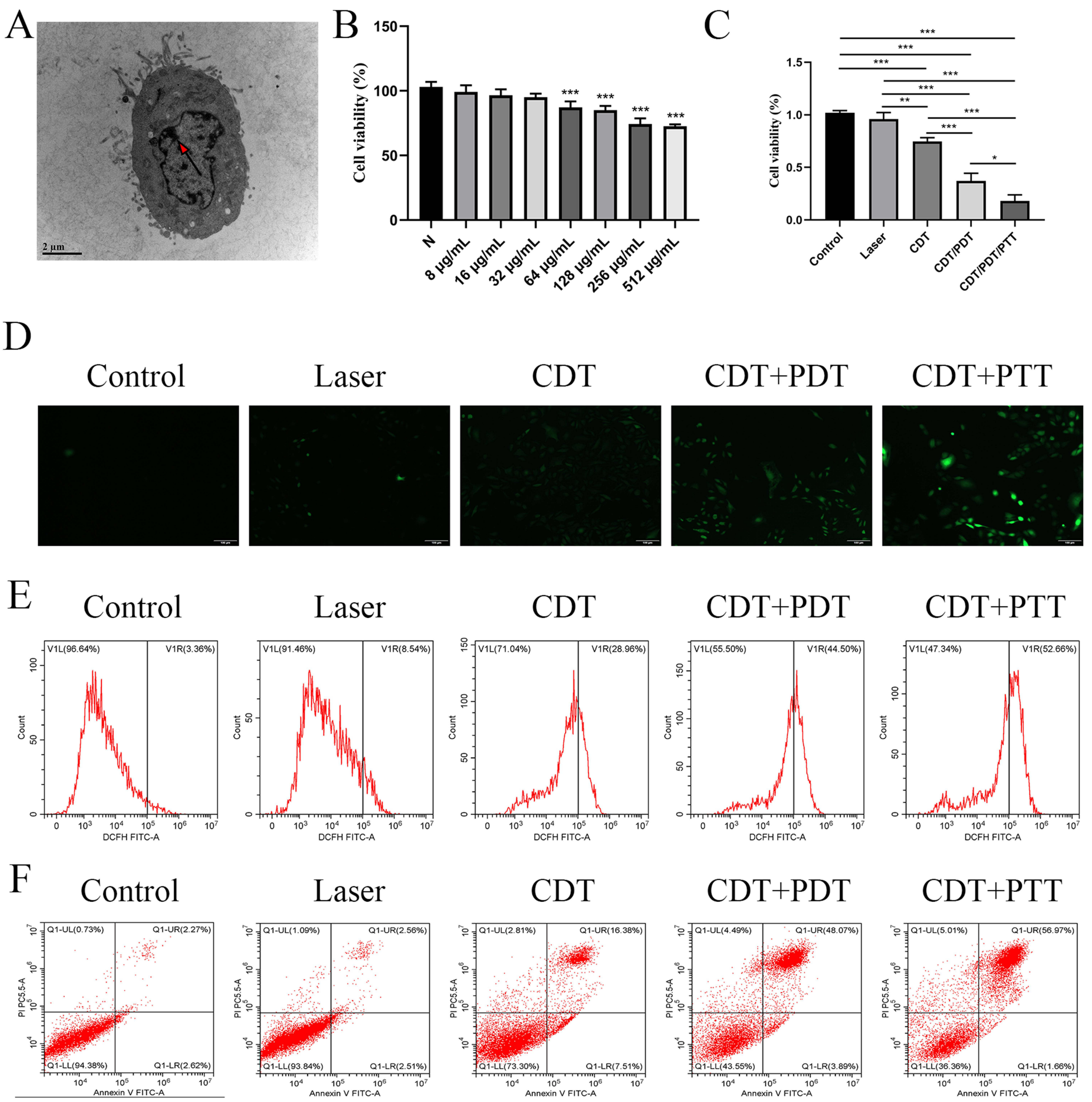

Figure 4 (**A**) Observation of endocytosis nanoparticles in MB49 cells by biological transmission electron microscopy. The red arrow indicates the $Cu_2(OH)PO_4$@PAA nanoparticles. (**B**) Cell viability of MB49 cell after incubation with different concentration of $Cu_2(OH)PO_4$@PAA aqueous solution for 4 h. (**C**) The cytotoxic effects of different treatments on MB49 cells were also assessed using CCK-8 method. (**D**) DCFH-DA was used as the fluorescence probe to detect intracellular ROS (scale bars: 100 μm). (**E**) DCFH-DA was used to detect intracellular ROS by Flow-cytometry analysis. (**F**) Flow cytometry apoptosis assays of MB49 cells co-labeled with annexin-FITC and PI after varying treatments. Statistical significance was denoted as follows: *$p < 0.05$, **$p < 0.01$, and ***$p < 0.001$.

additional ROS generation. Notably, the CDT/PTT group displayed the strongest fluorescence signal, indicating that under PTT-suitable temperatures, the highest ROS generation efficiency, mediated by the CDT/PDT properties of $Cu_2(OH)PO_4$@PAA, could be achieved. The trend of the quantitative data obtained by flow cytometry analysis was consistent with the above fluorescence results (Figure 4E). Flow cytometry apoptosis assays showed a consistent trend, with the highest apoptosis rate of MB49 tumor cells occurred in the CDT/PTT group (Figure 4F). Additionally, we used calcein-AM and PI to co-label MB49 cells in different groups, enabling visualization of live and dead cells to assess therapeutic efficacy. Compared with the overwhelming majority of bright green calcein-AM signals observed in the control and laser groups, both green calcein-AM and scattered red PI signals were visualized in the CDT group. Furthermore, with the appearance of PDT guided by mild warming and subsequent PTT induced by further warming, the red PI signal gradually filled the field of vision, whereas the green fluorescence signal disappeared (Figure 5A). These results further confirmed that the integration of CDT and phototherapy generates a potent therapeutic effect against MB49 cells, providing a theoretical foundation for the in vivo application of $Cu_2(OH)PO_4$@PAA.

Multimodal Therapy Inhibits EMT in vitro

Epithelial-mesenchymal transition (EMT) is a multistep biological process characterized by the loss of epithelial features and the acquisition of a mesenchymal phenotype, which is closely associated with tumor invasion and metastasis. In addition, several studies have demonstrated that the EMT is a pivotal process for anti-apoptosis, proliferation, stemness, and angiogenesis.[23] To elucidate whether the anti-tumor molecular mechanism of $Cu_2(OH)PO_4$@PAA is associated with EMT, we evaluated the expression of key EMT biomarkers using immunofluorescence. Given the high malignancy of MB49 cells and their weak E-cadherin expression, we increased the concentration of E-cadherin antibody and the incubation time to improve its expression level. Compared with the control group, the expression of the mesenchymal

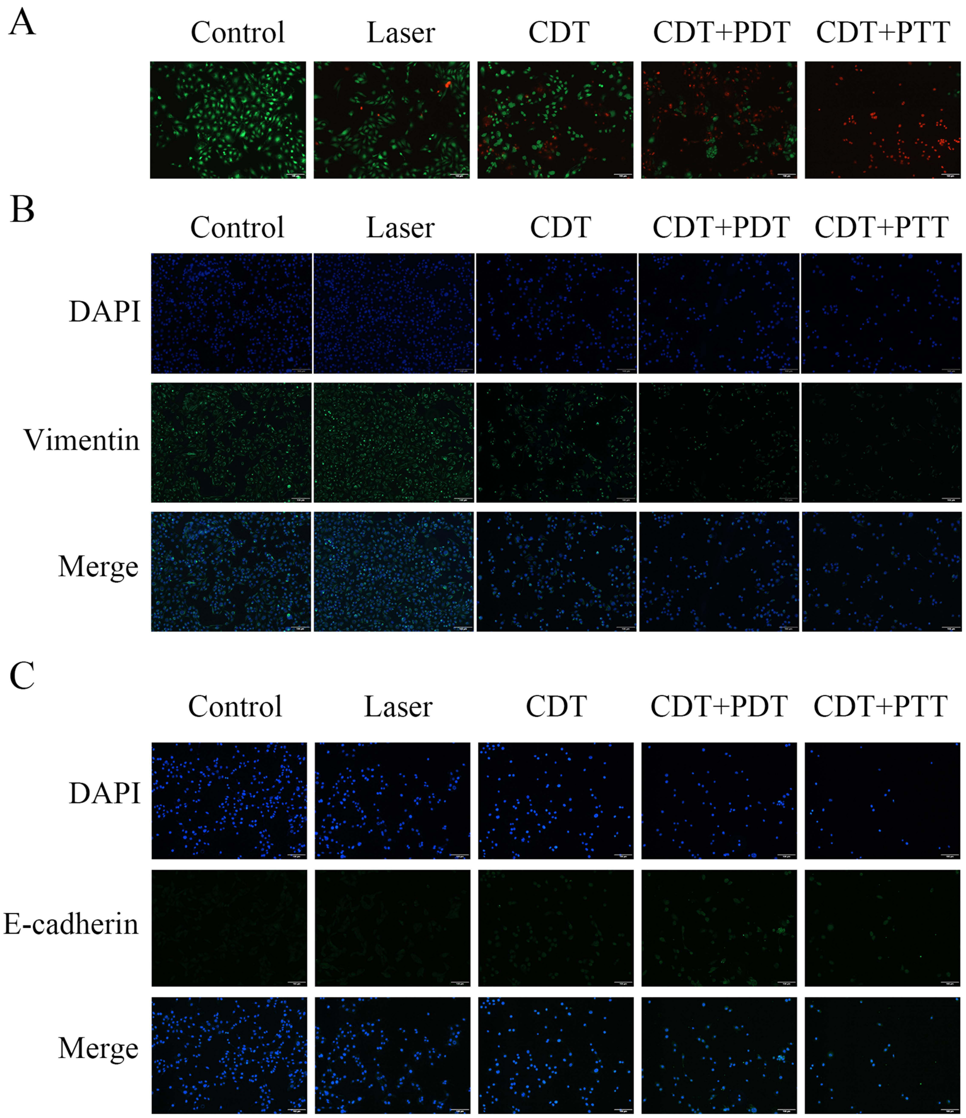

Figure 5 (**A**) Fluorescence images of MB49 cells co-labeled with calcein-AM and PI after varying treatments (scale bars: 100 μm). (**B** and **C**) The protein expression and subcellular localization of E-cadherin and Vimentin were detected by immunofluorescence assays in MB49 cells after different treatments (scale bars: 100 μm).

marker Vimentin decreased and the expression of the epithelial marker E-cadherin increased in the CDT group. Furthermore, with the sequential application of PDT and PTT, these changes become increasingly pronounced. These alterations in Vimentin and E-cadherin expression indicated that $Cu_2(OH)PO_4$@PAA could efficiently reverse EMT by ROS-based CDT/PDT and heating energy-based PTT (Figure 5B and C).

PA Imaging in vitro and in vivo

Photoacoustic (PA) imaging is an emerging tumor imaging modality with significant clinical potential owing to its unique advantages including noninvasiveness, high spatial resolution, and deep penetration. PA imaging is achieved by detecting ultrasonic waves generated by transient thermoelastic expansion in biological tissues or PA contrast agents upon laser irradiation.[24] The light-to-thermal energy conversion process in PA imaging is similar to that in PTT. As previously described, $Cu_2(OH)PO_4$@PAA nanoparticles have been proven to have high light absorption and excellent NIR radiation-induced hyperthermia. To evaluate their potential as exogenous PA contrast agents, we examined the photoacoustic signal transduction capability of $Cu_2(OH)PO_4$@PAA (Figure S8). The results revealed a prominent dose-dependent increase in the photoacoustic signal, which exhibited linear enhancement as the nanoparticle concentration increased from 0.03125 to 0.5 mg/mL (Figure 6A). MB49 tumor-bearing nude mice were intravenously administered $Cu_2(OH)PO_4$@PAA for in vivo PA imaging. We used ultrasound to locate the tumor site and recorded the PA signals of the tumor sites at different time points post injection. The PA signal at the tumor site emerged at 2 h, peaked at 4 h, and then gradually decreased (Figure 6B and C). The PA imaging performance of $Cu_2(OH)PO_4$@PAA nanoparticles highlights their high potential as PA imaging contrast agents, enabling detailed biomolecular information at the tumor site.

Multimodal Therapeutic Efficacy in vivo

The PDT and PTT anti-tumor efficacy of $Cu_2(OH)PO_4$@PAA in vivo was investigated in tumor-bearing mice. As shown in Figure 6D and E, compared with the laser-only group, the temperature at the tumor region in the PTT group rapidly reached 57.8 °C, which is suitable for hyperthermic ablation of tumor cells. Figure 7A shows a schematic of the in vivo experimental procedure. Tumor pictures (Figure 7B) were monitored after the administration of various treatments. As shown in Figure 7C, no evident differences in body weight were observed during the entire experimental period, indirectly indicating the therapeutic biosafety of $Cu_2(OH)PO_4$@PAA. Compared to the control group, tumor growth was slightly inhibited in the CDT group and moderately inhibited in the PDT group, whereas the strongest tumor suppression was observed in the PTT group (Figure 7D). The in vivo tumor volume showed a similar trend (Figure 7E). H&E staining was performed to observe the histological features of the tumor tissues in each group. The degree of tissue damage and necrosis in the CDT/PTT group was significantly greater than those in the CDT and CDT/PDT groups, whereas the laser group showed negligible cell damage (Figure 7F). TUNEL and PCNA assays were also conducted to assess the apoptosis and proliferation of tumor cells, respectively. The CDT/PTT group exhibited a higher number of apoptotic cells and a lower number of proliferating cells than the other groups did. Given that in vitro experiments demonstrated that $Cu_2(OH)PO_4$@PAA nanoparticles could inhibit EMT in MB49 tumor cells, the expression of tumor progression markers Vimentin and E-cadherin in xenograft tumors was further analyzed by immunohistochemistry (Figure 8A). The positive expression of Vimentin decreased and the expression of E-cadherin increased in the CDT group. When the tumor site was exposed to PDT or PTT caused by laser irradiation, this trend was more significant, especially in the CDT/PTT group. Therefore, it was concluded that $Cu_2(OH)PO_4$@PAA could provide a satisfactory in vivo tumor suppression effect by inhibiting cell proliferation and EMT and promoting cell apoptosis. Next, to evaluate the safety of $Cu_2(OH)PO_4$@PAA, after intravenous injection of the $Cu_2(OH)PO_4$@PAA nanoparticles for 0, 1, 3, 5, 7, and 14 days, we collected the major organs (the heart, liver, spleen, lungs, and kidneys) of the mice for H&E staining. Figure 8B shows no detectable histopathological damage in any of the organs. In addition, blood biochemical indices and routine blood analyses revealed no signs of toxicity in mice at the tested doses throughout the observation period (Figure 8C). These results demonstrated that $Cu_2(OH)PO_4$@PAA can be safely used as a nanotherapeutic reagent for in vivo imaging and treatment.

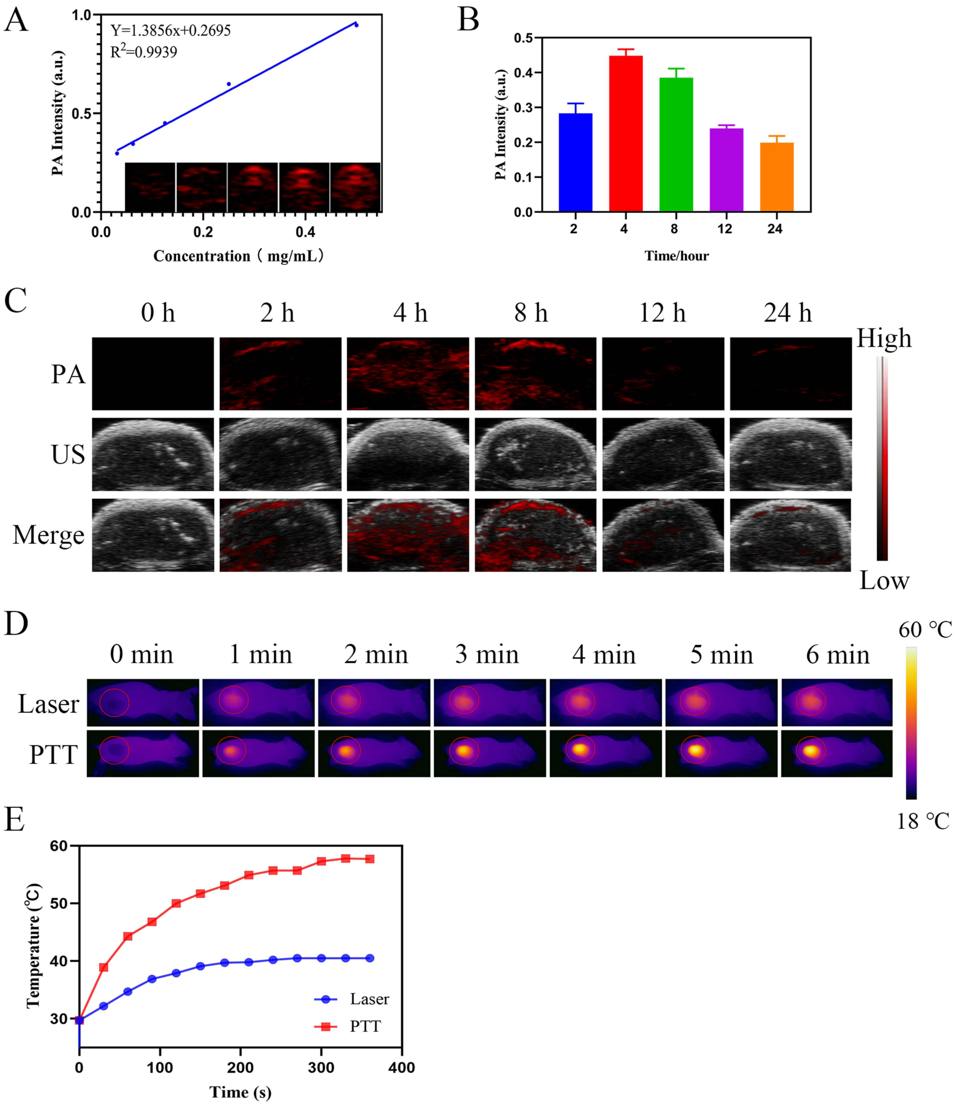

Figure 6 (**A**) In vitro PA images and PA values of Cu$_2$(OH)PO$_4$@PAA at different concentrations. (**B**) PA intensity values at tumor regions in MB49 tumor-bearing mice after varied treatment durations. (**C**) In vivo PA image of tumor regions in MB49 tumor-bearing mice at different time points after Cu$_2$(OH)PO$_4$@PAA dispersion injection. (**D**) Infrared thermal image changes at tumor regions of different treatment group. (**E**) Temperature change curves at tumor regions of the different treatment group.

Discussion

Bladder cancer (BC), one of the most common malignancies of the urinary system, poses a significant threat to human life and health.[2] Conventional treatments include surgical resection, radiotherapy and chemotherapy.[5] However, the existing dominant treatment methods have a series of defects. For instance, transurethral resection of bladder tumors often results in residual lesions, radical cystectomy causes substantial physical trauma to patients, and chemotherapeutic drugs, which suffer from limited bioavailability, frequently develop multidrug resistance.[1,5] Consequently, BC continues to face challenges such as high rates of recurrence and metastasis.[5] A new type of anti-bladder tumor therapy that can not only compensate for the disadvantages of existing treatments but also be more effective is urgently needed.

In recent years, the field of nanoparticle-targeted anti-tumor therapy has developed rapidly, with numerous minimally invasive or noninvasive nanoparticles being developed to integrate multiple innovative therapeutic approaches.[25] Nanoparticles based on improving the level of intracellular ROS have been widely studied because ROS, with strong oxidation and high genotoxicity, can lead to tumor cell necrosis and apoptosis by promoting organelle damage, oxidative DNA damage, immune damage, and cell cycle arrest.[26,27] Nanoparticles containing metal ions (such as iron, copper, and manganese) can transform endogenous H_2O_2 into •OH by triggering an ion-activated Fenton-like effect to improve the

https://doi.org/10.2147/IJN.S534840

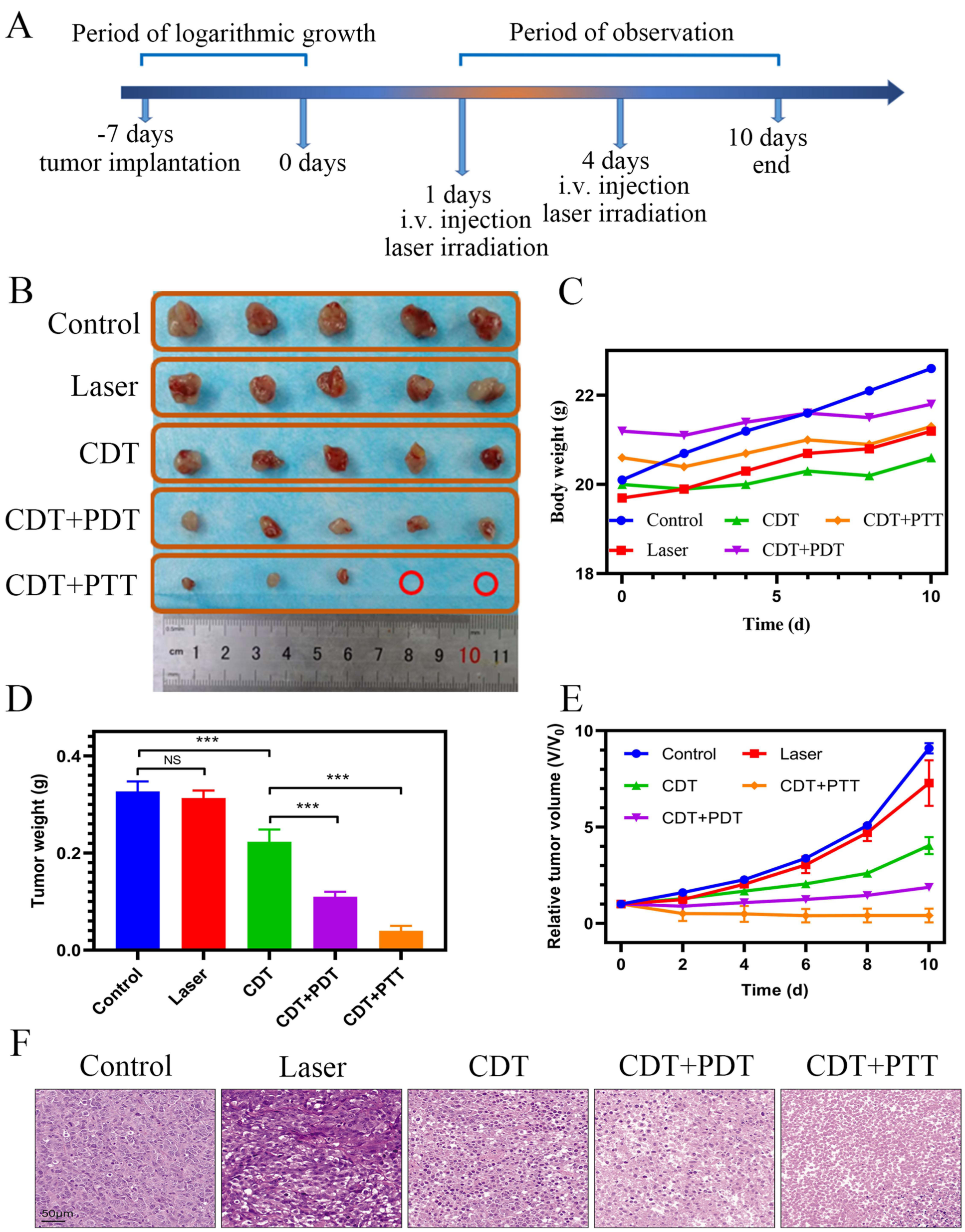

Figure 7 (**A**) Schematic illustration of the in vivo experimental design. (**B**) Photographs of tumors dissected from mice of five groups after different treatments. The red circles indicate that the tumors have disappeared after treatment. (**C**) Body-weight curves of five groups after various treatments (n = 5). (**D**) Weight of tumors after various treatments (n = 5). (**E**) Quantitative measurements of tumor volume of mice after various treatments. (**F**) H&E staining analysis of tumor tissues in all treatment groups (scale bars: 50 μm). NS: No statistical significance, and *** indicates $p < 0.001$.

intracellular ROS level are highly valued.[15,18] This ROS-mediated tumor chemotherapy process facilitated by ion-based nanoparticles is called CDT and is recognized as a novel noninvasive treatment method for cancer.[21] PDT, another typical ROS-mediated anti-tumor treatment, primarily relies on the conversion of triplet oxygen to cytotoxic $^1O_2$ by photosensitive nanoparticles under external light irradiation.[27] Although combining CDT and PDT has been shown to enhance ROS generation in several studies, the practical application of this combined therapy is still restricted either by restricted ROS generation due to the hypoxic state of the tumor microenvironment and attenuation of light energy penetration or by the short half-life and limited diffusion range of ROS itself.[17,28]

PTT, an anti-tumor approach based on light-to-heat conversion, is promising for synergistically enhancing the effects of CDT and PDT. This is because its thermal effects on tumor sites may improve blood flow and oxygen supply, thereby addressing hypoxic conditions that limit ROS generation.[29] Xiang et al developed a trifunctional theranostic FeWOx-

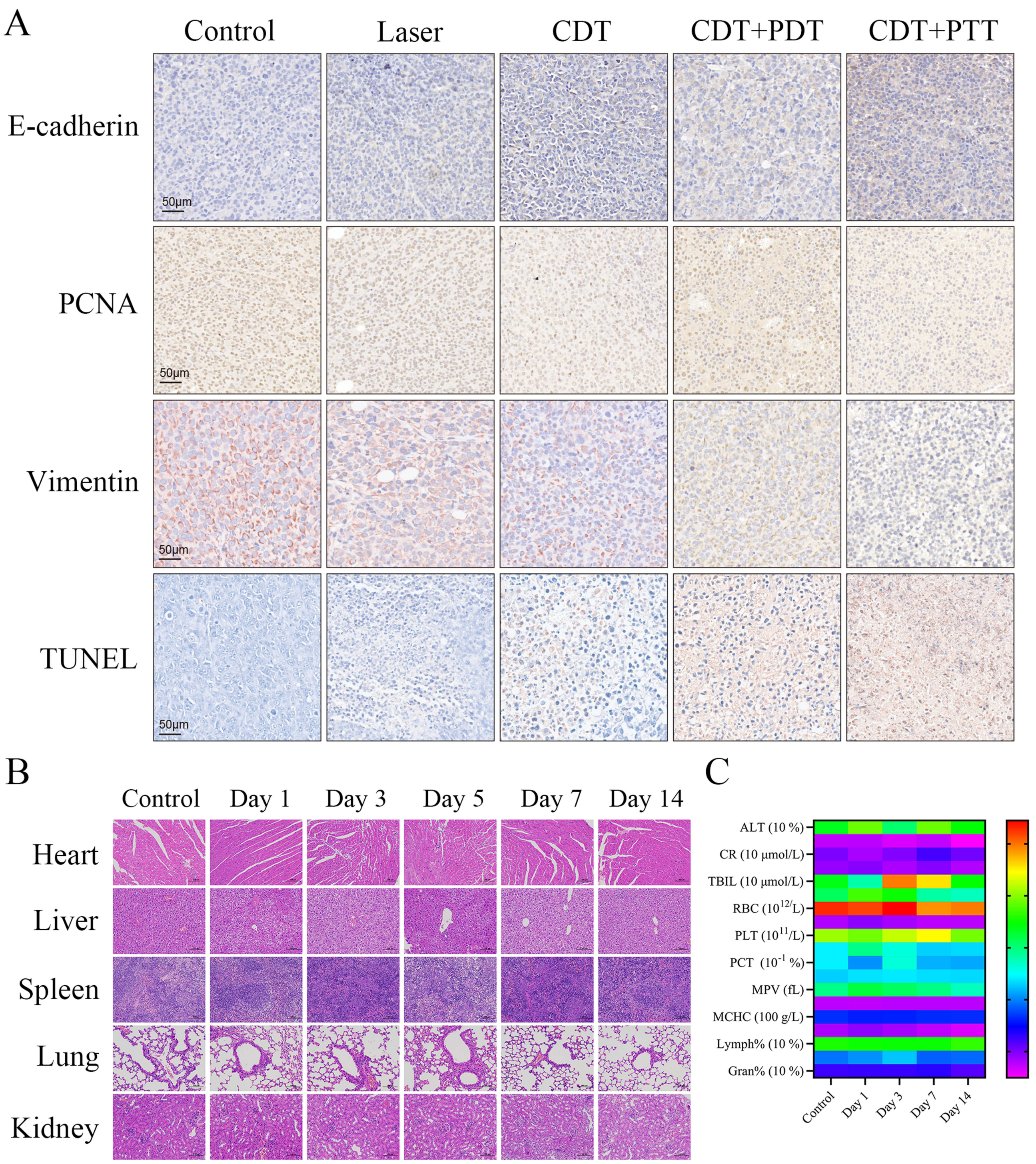

Figure 8 (**A**) Immunohistochemical analysis of E-cadherin, PCNA, Vimentin and TUNEL staining at tumor sites after various treatments (scale bars: 50 μm). (**B**) H&E staining of the major organs at corresponding time intervals. (**C**) Hematological and blood biochemical test of mice after intravenous injection of $Cu_2(OH)PO_4$@PAA at different time intervals.

PEG nanoadjuvant and demonstrated that the strongest tumor suppression effect of this nanoparticle appeared in the CDT/PTT combined treatment group in vivo and in vitro, highlighting the high efficacy of multimodal therapeutic strategies.[30] This is consistent with our study, in which the PTT group exhibited the best antitumor efficacy. Furthermore, PTT nanoparticles typically exhibit excellent NIR absorption properties and strong photothermal conversion capabilities, which are prerequisites for integrating tumor imaging diagnosis with real-time guided therapy. This is because the underlying mechanism of PA imaging relies on the photo-to-heat-to-acoustic wave conversion excited by NIR.[31]

Inspired by these findings, we established a PAA-modified copper-based nanoparticle ($Cu_2(OH)PO_4$@PAA) that can combine CDT/PTT effects to effectively eliminate bladder cancer under laser irradiation in the NIR-I biological window. Additionally, the paramagnetic properties, laser absorption characteristics, and typical enhanced permeability and retention (EPR) effect of Cu_2(OH)PO4@PAA promoted the accumulation of these nanoparticles in tumor regions, enabling their application in PA imaging.

A simple and reproducible hydrothermal method was employed to synthesize $Cu_2(OH)PO_4$@PAA, which provided a foundation for its potential widespread clinical application. Immediately after preparation, we characterized the physicochemical properties of $Cu_2(OH)PO_4$@PAA. PAA was introduced to modify the surface and reduce the size of $Cu_2(OH)PO_4$. TEM and SEM showed that $Cu_2(OH)PO_4$ has a typical spherical structure, as described in previous studies. The modification with PAA has been proven by others to enhance the biocompatibility of nanoparticles in the bloodstream.[32] Our study also confirmed that PAA modification effectively prevented significant precipitation and aggregation of $Cu_2(OH)PO_4$, thereby potentially enhancing their stability for in vivo delivery applications. Nanoparticles can preferentially accumulate in tumors through the EPR effect.[33] The average size of the synthesized $Cu_2(OH)PO_4$@PAA in this study allowed these nanoparticles to traverse the endothelial gaps in tumors, facilitating their accumulation at the tumor sites. To evaluate whether $Cu_2(OH)PO_4$@PAA was excited by laser irradiation and its optical absorption properties were investigated. The broad absorption spectrum of $Cu_2(OH)PO_4$@PAA, ranging from 500 to 1600 nm, encompasses the NIR-I biological window (750–950 nm), demonstrating its potential for NIR-I laser-induced photothermal or photodynamic conversion. Next, we evaluated the ROS generation capability of $Cu_2(OH)PO_4$@PAA in vitro. Overexpression of reduced GSH is a characteristic of the TME, which can counteract the production of ROS and hinder ROS-dependent anti-tumor effects.[34] However, the change in the DTNB absorption curve showed that $Cu_2(OH)PO_4$@PAA oxidized GSH in a time-dependent manner, indicating its ability to enhance ROS-mediated cytotoxicity by acting as a glutathione oxidase mimic to deplete GSH. Both CDT and PDT are ROS-related anti-tumor strategies, however, the types of ROS involved in these two approaches are different. The realization of the CDT property mainly depends on the conversion of H_2O_2 into •OH by Cu^+ (the reduced product of Cu^{2+} mediated by GSH), whereas the PDT effect is predominantly driven by the photogeneration of $^1O_2$. The changes in the absorption curves using the •OH indicator TMB and $^1O_2$ indicator DPBF confirmed that $Cu_2(OH)PO_4$@PAA effectively induced both the CDT and PDT effects.

We also tested the PTT performance of $Cu_2(OH)PO_4$@PAA nanoparticles by treating MB49 cells with different concentrations and laser power densities, and found that the synthesized $Cu_2(OH)PO_4$@PAA could act as a potent NIR-I-triggered PTT agent. Photostability is a critical factor that determines the durability of the photothermal conversion in nanoparticles. After five on/off cycles of NIR laser irradiation, $Cu_2(OH)PO_4$@PAA exhibited an excellent photostability. The targeted killing of tumor cells rather than normal cells is a prerequisite for the clinical application of nanoparticles. To identify the optimal concentration that balances cytotoxicity against tumor cells and biosafety for normal cells, HUVEC and MB49 cells were incubated with varying concentrations of $Cu_2(OH)PO_4$@PAA. Subsequently, the ROS generation and apoptosis-inducing effects of CDT, PDT, and PTT, either individually or in combination, were evaluated in a cell experiment. Consistent with previous reports, the single CDT effect of these metal-based nanoparticles inhibited tumors through ROS generation; however, the combination of CDT, PDT, and PTT produced a significantly stronger synergistic anti-tumor effect.

Previous studies have demonstrated that the high recurrence and progression rates of bladder cancer are closely associated with EMT.[35] Therefore, we evaluated the effect of $Cu_2(OH)PO_4$@PAA on EMT. As expected, with the sequential introduction of CDT, PDT, and PTT, vimentin-positive cells gradually decreased, whereas E-cadherin-positive cells gradually increased, confirming that $Cu_2(OH)PO_4$@PAA possesses anti-EMT function.

Given that the photothermal properties of copper-based nanomaterials have been confirmed by our experiments and others,[36] we assessed the PA-imaging performance of $Cu_2(OH)PO_4$@PAA. In vitro experiment showed its outstanding PA imaging capability, which exhibited a positive correlation with the nanoparticle concentration. Additionally, we monitored PA signals at tumor sites at different time points following the intravenous injection of $Cu_2(OH)PO_4$@PAA. Specific imaging of tumor regions suggested that $Cu_2(OH)PO_4$@PAA can serve as an effective strategy for visualizing the treatment process.

As last, inspired by the excellent in vitro anti-tumor capability of the $Cu_2(OH)PO_4$@PAA, we investigated in vivo anti-tumor effects using an MB49 xenograft model in nude mice. The CDT condition was achieved by intravenous injection of $Cu_2(OH)PO_4$@PAA nanoparticles without a laser, whereas the PDT and PTT conditions were established by controlling the temperature at the tumor site. The PTT condition, which requires the tumor temperature to exceed 42 °C to induce cell death, was confirmed by temperature curves showing distinct thermal profiles under the two laser-induced conditions. The heat generated during PTT was sufficient to kill tumor cells. Similar to in vitro results, the single CDT effect of $Cu_2(OH)PO_4$@PAA inhibited the increase in tumor weight, and further induction of PDT by laser irradiation enhanced this inhibition effect. As for the anti-tumor mechanism, the changes in cell apoptosis, proliferation, and EMT of tumor sites in each group of mice revealed by histopathological examination could explain the difference in the tumor inhibition effect. There were no significant changes in the weight of the mice, and there were no injurious changes in H&E staining of the main organs and blood tests, confirming the excellent biosafety and minimal toxicity of $Cu_2(OH)PO_4$@PAA. These findings highlight the potential feasibility of this method for clinical application.

While this study provides valuable proof-of-concept for phototherapeutic strategies in bladder cancer, several limitations should be acknowledged. Specifically, we only validated our approach in a subcutaneous tumor model in mice and did not construct an orthotopic bladder cancer model, which restricts the ability to fully replicate the clinical treatment process and its potential outcomes. Additionally, the nanomaterials employed were repurposed from existing systems rather than being newly engineered. To further enhance the therapeutic effects in the future, the development of custom-designed nanomaterials with enhanced targeting ability, superior biocompatibility, and improved in vivo degradation and metabolism is warranted.

Conclusion

In this study, we developed a PAA-coated $Cu_2(OH)PO_4$ nanoparticle using the hydrothermal method following previously reported protocols, which was used as an imaging-guided tumor therapeutic agent for bladder cancer. This nanoparticle with a strong NIR light absorption ability was demonstrated to not only implement the CDT effect by yielding cytotoxic ·OH through a Cu^+-induced Fenton-like reaction and obvious depletion of GSH, but also achieve synergistic photodynamic and photothermal effects through ROS production and heat energy conversion under laser irradiation. Investigations into the anti-tumor mechanisms, both in bladder cancer cells and in mouse xenograft models, illustrated that $Cu_2(OH)PO_4$@PAA-mediated CDT/PDT/PTT effects are achieved by inducing cell apoptosis, inhibiting EMT and cell proliferation. Moreover, the major organs of mice injected with nanoparticles showed no significant pathological changes, demonstrating the high biosafety of $Cu_2(OH)PO_4$@PAA and its strong potential for clinical translation. Additionally, owing to its photothermal properties, $Cu_2(OH)PO_4$@PAA can be utilized for in vivo PA imaging of tumor sites via intravenous injection to realize precise imaging-guided tumor ablation. In summary, $Cu_2(OH)PO_4$@PAA is a multifunctional theranostic nanoparticle that integrates ROS-mediated CDT/PDT with laser-related PTT for tumor imaging and treatment.

Acknowledgments

The authors are grateful to the State Key Laboratory of Ultrasound in Medicine and Engineering for providing experimental equipment and facilities.

Funding

This work was supported by the China Postdoctoral Science Foundation (Grant No. 2021MD703925), Chongqing Postdoctoral Research Special Funding Project (Grant No. 2112012723387098), and the Zhejiang Natural Science Foundation (Grant No. LTGY24H160005), Ningbo Natural Science Foundation (Grant No. 2022J218, 2022J217, and 2023J018), Ningbo Health and Medical Science and Technology Program (No. 2023Y09), Ningbo Public Welfare Technology Research Program (Grant No.2023S025), Zhejiang Provincial Foundation for Medical and Health Sciences (Grant Nos.2024KY305 and 2024KY1514), Basic Research Project of Shanxi Province (grant No. 20210302123259), Doctoral Research Project of Shanxi Medical University (grant No. XD1901), Ningbo Top Medical and Health Research Program (2022020203), and Zhejiang Engineering Research Center of Innovative technologies and diagnostic and therapeutic equipment for urinary system diseases.

Disclosure

The authors declare that they have no competing interests.

References

1. Holzbeierlein JM, Bixler BR, Buckley DI, et al. Diagnosis and treatment of non-muscle invasive bladder cancer: AUA/SUO guideline: 2024 amendment. *J Urol*. 2024;211(4):533–538. doi:10.1097/JU.0000000000003846
2. Dyrskjøt L, Hansel DE, Efstathiou JA, et al. Bladder cancer. *Nat Rev Dis Primers*. 2023;9(1):58. doi:10.1038/s41572-023-00468-9
3. Boschi F, Malatesta M. Nanoparticle-based techniques for bladder cancer imaging: a review. *Int J Mol Sci*. 2023;24(4):3812. doi:10.3390/ijms24043812
4. Qiu HP, Wang JW, Zhi Y, et al. Hyaluronic acid-conjugated fluorescent probe-shielded polydopamine nanomedicines for targeted imaging and chemotherapy of bladder cancer. *ACS Appl Mater Interfaces*. 2023;15(40):46668–46680. doi:10.1021/acsami.3c09564
5. Lopez-Beltran A, Cookson MS, Guercio BJ, et al. Advances in diagnosis and treatment of bladder cancer. *BMJ*. 2024:384:e076743. doi:10.1136/bmj-2023-076743
6. Teoh JYC, Kamat AM, Black PC, et al. Recurrence mechanisms of non-muscle-invasive bladder cancer - a clinical perspective. *Nat Rev Urol*. 2022;19(5):280–294. doi:10.1038/s41585-022-00578-1
7. Doeveren TV, Remmers S, Boevé ER, et al. Intravesical instillation of chemotherapy before radical surgery for upper urinary tract urothelial carcinoma: the REBACARE Trial. *Eur Urol*. 2025;87(4):444–452. doi:10.1016/j.eururo.2024.12.006
8. Fang LP, Chen ZZ, Dai JN, et al. Recent advances in strategies to enhance photodynamic and photothermal therapy performance of single-component organic phototherapeutic agents. *Adv Sci (Weinh)*. 2025;12(7):e2409157. doi:10.1002/advs.202409157
9. Ji B, Wei M, Yang B. Recent advances in nanomedicines for Photodynamic Therapy (PDT)-driven cancer immunotherapy. *Theranostics*. 2022;12(1):434–458. doi:10.7150/thno.67300
10. Li XT, Chen L, Huang MT, et al. Innovative strategies for photodynamic therapy against hypoxic tumor. *Asian J Pharm Sci*. 2023;18(1):100775. doi:10.1016/j.ajps.2023.100775
11. Wang Y, Xu YY, Song JY. Tumor cell-targeting and tumor microenvironment-responsive nanoplatforms for the multimodal imaging-guided photodynamic/photothermal/chemodynamic treatment of cervical cancer. *Int J Nanomed*. 2024;19:5837–5858. doi:10.2147/IJN.S466042
12. Zhang Z, Yue X, Lan N, et al. Effective antitumor synergistic treatment with fiber-photothermal therapy and heat shock protein inhibitors. *ACS Appl Mater Interfaces*. 2025;17(3):4368–4379. doi:10.1021/acsami.4c11734
13. Wei K, Wu Y, Zheng X. A light-triggered J-aggregation-regulated therapy conversion: from photodynamic/photothermal therapy to long-lasting chemodynamic therapy for effective tumor ablation. *Angew Chem Int Ed Engl*. 2024;63(23):e202404395. doi:10.1002/anie.202404395
14. Dong Q, Wang J, Liu JH, et al. Manganese-based redox homeostasis disruptor for inducing intense ferroptosis/apoptosis through xCT inhibition and oxidative stress injury. *Adv Healthc Mater*. 2023;12(28):e2301453. doi:10.1002/adhm.202301453
15. Sun DQ, Sun XX, Zhang X, et al. Emerging chemodynamic nanotherapeutics for cancer treatment. *Adv Healthc Mater*. 2024;13(22):e2400809. doi:10.1002/adhm.202400809
16. Liu SW, Han S, Song YZ, et al. Disulfide-bridged dendritic organosilicas-based biodegradable molecularly imprinted polymers for multiple targeting and pH/redox-responsive drug release toward chemical/photodynamic synergistic tumor therapy. *Adv Healthc Mater*. 2023;12(20):e2300184. doi:10.1002/adhm.202300184
17. Wang X, Peng JL, Meng C, et al. Recent advances for enhanced photodynamic therapy: from new mechanisms to innovative strategies. *Chem Sci*. 2024;15(31):12234–12257. doi:10.1039/d3sc07006a
18. Wu WC, Pu YY, Shi JL. Nanomedicine-enabled chemotherapy-based synergetic cancer treatments. *J Nanobiotechnology*. 2022;20(1):4. doi:10.1186/s12951-021-01181-z
19. Chen YD, Liu PF, Sun P, et al. Oncogenic MSH6-CXCR4-TGFB1 feedback loop: a novel therapeutic target of photothermal therapy in glioblastoma multiforme. *Theranostics*. 2019;9(5):1453–1473. doi:10.7150/thno.29987
20. Guo W, Qiu ZY, Guo CS, et al. Multifunctional theranostic agent of Cu2(OH)PO4 quantum dots for photoacoustic image-guided photothermal/photodynamic combination cancer therapy. *ACS Appl Mater Interfaces*. 2017;9(11):9348–9358. doi:10.1021/acsami.6b15703
21. Jia CY, Guo YX, Wu FG. Chemodynamic therapy via fenton and fenton-like nanomaterials: strategies and recent advances. *Small*. 2022;18(6):e2103868. doi:10.1002/smll.202103868
22. Lapenna D. Glutathione and glutathione-dependent enzymes: from biochemistry to gerontology and successful aging. *Ageing Res Rev*. 2023;92:102066. doi:10.1016/j.arr.2023.102066
23. Glaviano A, Lau HSH, Carter LM, et al. Harnessing the tumor microenvironment: targeted cancer therapies through modulation of epithelial-mesenchymal transition. *J Hematol Oncol*. 2025;18(1):6. doi:10.1186/s13045-024-01634-6
24. Kubelick KP, Kim J, Kim M, et al. In vivo ultrasound and photoacoustic imaging of nanoparticle-engineered t cells and post-treatment assessment to guide adoptive cell immunotherapy. *ACS Nano*. 2025;19(6):6079–6094. doi:10.1021/acsnano.4c12929
25. Guo XL, Yang ND, Ji WH, et al. Mito-bomb: targeting mitochondria for cancer therapy. *Adv Mater*. 2021;33(43):e2007778. doi:10.1002/adma.202007778
26. Guo QY, Tang YN, Wang SM, et al. Applications and enhancement strategies of ROS-based non-invasive therapies in cancer treatment. *Redox Biol*. 2025;80:103515. doi:10.1016/j.redox.2025.103515
27. Wang HY, Qiao C, Guan QT, et al. Nanoparticle-mediated synergistic anticancer effect of ferroptosis and photodynamic therapy: novel insights and perspectives. *Asian J Pharm Sci*. 2023;18(4):100829. doi:10.1016/j.ajps.2023.100829
28. Li JL, Li B, Liu F, et al. A multifunctional nanosystem catalyzed by cascading natural glucose oxidase and Fe_3O_4 Nanozymes for synergistic chemodynamic and photodynamic cancer therapy. *Acta Biomater*. 2024;190:518–530. doi:10.1016/j.actbio.2024.10.024
29. Yin Y, Wong KH, Wen L, et al. Active Iron-drug nanocomplexes improve photodynamic and photothermal cancer therapy by mitigating tumor hypoxia and counteracting tumor heat resistance. *Adv Healthc Mater*. 2025;18(13):e2107809. doi:10.1002/adhm.202404485
30. Xiang QY, Yang C, Luo Y, et al. Near-infrared ii nanoadjuvant-mediated chemodynamic, photodynamic, and photothermal therapy combines immunogenic cell death with PD-L1 blockade to enhance antitumor immunity. *Small*. 2022;18(13):e2107809. doi:10.1002/smll.202107809

31. Repetowski P, Warszyńska M, Dąbrowski JM. NIR-activated multifunctional agents for the combined application in cancer imaging and therapy. *Adv Colloid Interface Sci*. 2025;336:103356. doi:10.1016/j.cis.2024.103356
32. Arkaban H, Barani M, Akbarizadeh MR, et al. Polyacrylic acid nanoplatforms: antimicrobial, tissue engineering, and cancer theranostic applications. *Polymers*. 2022;14(6):1259. doi:10.3390/polym14061259
33. Yang C, Ming H, Li B, et al. A pH and glutathione-responsive carbon monoxide-driven nano-herb delivery system for enhanced immunotherapy in colorectal cancer. *J Control Release*. 2024;376:659–677. doi:10.1016/j.jconrel.2024.10.043
34. Hao CQ, Shao YT, Tian JR, et al. Dual-responsive hollow mesoporous organosilicon nanocarriers for photodynamic therapy. *J Colloid Interface Sci*. 2024;659:582–593. doi:10.1016/j.jcis.2024.01.034
35. Qin JK, Liao KC, Huang L, Qiu R, Tang N, Wu J. Huang L, et al. proteome-driven transcriptomic dissection of emt networks in bladder cancer based on the VIM and CDH2 protein macromolecules influence: from molecular-protein subtyping to therapeutic target prioritization. *Int J Biol Macromol*. 2025;315(Pt 2):144585. doi:10.1016/j.ijbiomac
36. Zuo WB, Fan ZX, Chen LP, et al. Copper-based theranostic nanocatalysts for synergetic photothermal-chemodynamic therapy. *Acta Biomater*. 2022;147:258–269. doi:10.1016/j.actbio.2022.05.030